Friction

Research Article

Atomistic study of material removal behavior during ultrasonic vibration-assisted nanoscratching of single-crystal AlN

Shuaicheng Feng[1], Jian Guo[1,✉], Jiaqin Yin[1], Hanqiang Wu[2], Linmao Qian[3], Chen Xiao[3,4,✉]

Cite this article: Feng SC, Guo J, Yin JQ, et al. *Friction* 2026, **14**(3): 9441097. https://doi.org/10.26599/FRICT.2025.9441097

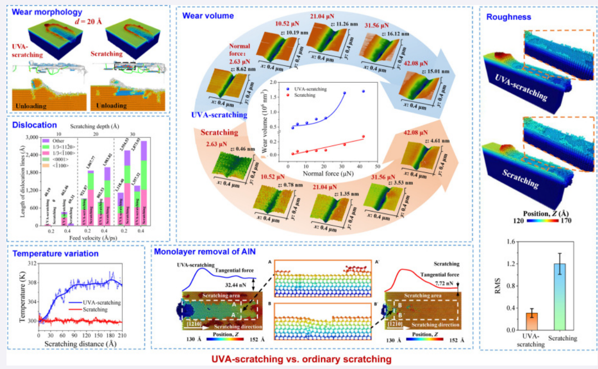

ABSTRACT: Molecular dynamics simulations were used to investigate surface material removal and subsurface damage at the nanoscale to the atomic scale during ultrasonic vibration-assisted (UVA) nanoscratching of single-crystal AlN with a single-point diamond tip. The simulation results suggest that UVA-scratching results in a lower tangential force, normal force, and friction coefficient than ordinary scratching at the same scratch depth. UVA-scratching results in a greater material removal rate than ordinary scratching because of the vibration-induced rise in the local temperature, which facilitates atomic bond breakage and the lateral extension of stacking faults in the superficial layer. Uniform monolayer removal consisting of the outermost Al atoms and the connected N atoms is easier to achieve in the scratching path with the UVA-scratching mode than with the ordinary scratching mode. UVA-scratching produces a smoother scratched surface. For example, the root mean square of the surface after UVA-scratching is only approximately one-third of that after ordinary scratching at the same scratch depth. Furthermore, ultrasonic vibration can reduce scratching-induced material pile-up and subsurface damage, which primarily consists of dislocations and stacking faults. This is because vibration can reduce the stress distribution range and restrain the stress concentration. This work can provide useful knowledge for high-quality and efficient ultraprecision surface machining for hard-brittle materials.

KEYWORDS: ultrasonic vibration-assisted (UVA) nanoscratching; removal mechanism; subsurface damage; monolayer removal; molecular dynamics

1 Introduction

Ultraprecision surface machining methods can be divided into single-point and surface processing methods according to the motion of the machining tool and the material removal method of the target workpiece [1–6]. Its purpose is to achieve controlled processing of ultrahigh-precision surfaces or structures by precisely controlling the minimal removal of materials that can reach the atomic scale. Typical ultraprecision machining techniques, such as single-point diamond turning, scanning probe microscopy-based scratching, chemical–mechanical polishing (CMP), and ultraprecision grinding, play significant roles in semiconductor processing [7–12]. Owing to its bandgap, high thermal conductivity, and excellent mechanical and piezoelectric properties [13–15], single-crystal AlN has become an ideal substrate for the epitaxial growth of GaN, AlN, and AlGaN materials [16–18], an electronic packaging material for ultraviolet light-emitting diodes [19] and an excellent protective coating material in engineering applications [20]. High-end AlN-based wide bandgap semiconductor devices demand ultrasmooth, damage-free AlN substrates or wafers. Achieving such surfaces requires grinding and polishing processes, while the efficiency and quality of the subsequent CMP process are highly dependent on the results of the previous processing. The surface processing of hard-brittle semiconductor materials using traditional grinding and rubbing methods suffers from a low material removal rate and difficulties in controlling machining damage. To this end, researchers have proposed the utilization of external field-assisted methods, such as laser-assisted, plasma-assisted, and ultrasonic vibration-assisted methods, to improve the processing efficiency and quality [21]. Among them, the laser-assisted method causes material softening first by laser heating and then mechanically achieves a high removal rate to improve processing efficiency [22]. The plasma-assisted method modifies the material surface by injecting high-energy ions and hence can increase the removal rate and machinability of the target material, but ion implantation

[1] School of Mechanical Engineering, University of South China, Hengyang 421001, China. [2] Department of Mechanical and Energy Engineering, Southern University of Science and Technology, Shenzhen 518055, China. [3] Tribology Research Institute, State Key Laboratory of Rail Transit Vehicle System, Southwest Jiaotong University, Chengdu 610031, China. [4] Research Institute of Frontier Science, Southwest Jiaotong University, Chengdu 610031, China.

✉ Corresponding authors. E-mail: J. Guo, jguo@usc.edu.cn; C. Xiao, xiaochenswjtu93@gmail.com

Received: September 16, 2024; Revised: December 26, 2024; Accepted: March 18, 2025

contamination cannot be completely ignored [23]. Moreover, by utilizing a transducer to convert high-frequency electrical energy into high-frequency mechanical vibration energy, the ultrasonic vibration-assisted (UVA) processing method has become a good candidate for obtaining high processing efficiency and low damage to many hard-brittle materials. The material removal during UVA processing is attributed primarily to the synergistic effects of material softening caused by high-frequency vibration and periodic vibration impacts [24].

Recently, several studies have shown that ultrasonic vibration can effectively improve the material removal rates of Si, SiC, sapphire, GaN, and other hard-brittle materials and reduce subsurface damage during ultraprecision surface machining [25–29]. For example, Qiao et al. [30] indicated that ultrasonic vibration increases the critical load of the brittle–ductile transition of ceramic materials and promotes the propagation of shallow lateral cracks to the surface, thereby improving the material removal efficiency in the scratching process. Wang et al. [31] reported that during UVA cutting, the main defects in the subsurface are lateral microcracks that propagate mainly toward the free surface, thus promoting material removal. Ultrasonic vibration can also prevent the median crack from extending toward the bulk material, which contributes to improving the uniformity of groove quality. Note that material removal during UVA machining in the above studies falls into the multiasperity condition, where the propagation of lateral cracks is the main cause of vibration-enhanced material removal. Nevertheless, the relatively limited understanding of the UVA material removal mechanism of AlN severely restricts the development of AlN UVA ultraprecision machining technology.

Given the experimental difficulty in terms of accuracy and control, current research on nanoscale UVA surface machining is primarily based on molecular dynamics (MD) simulations. Using interatomic interactions, MD simulations can assess nanoscale to atomic-scale force–heat behavior, structural transitions of materials, and material attrition under various mechanical conditions [32, 33]. Through MD simulations of UVA cutting, Liu et al. [34] reported that crack generation and propagation can be effectively suppressed by increasing the cutting temperature via vibration. Using MD simulations, Wang et al. [35, 36] investigated the surface formation mechanism during UVA cutting of tungsten. They demonstrated that, compared with the ordinary cutting method, this cutting approach can improve the quality of the machined surface, resulting in strong plastic flow features and undamaged tungsten particles. Zhang et al. [37, 38] carried out a study of laser and ultrasonic vibration-assisted nanogrinding for AlN. These results indicate that the coupling effect of lasers and vibration can increase the temperature of the nanogrinding area and reduce the hardness of the material, thus improving the processing efficiency and quality and reducing the subsurface damage. Tip-based nanofabrication methods, primarily atomic force microscopy (AFM), have attracted much attention from researchers because of their flexibility and high resolution. For instance, Wang et al. [39–41] investigated and proposed a tip-based ultrasonic vibration-assisted nanomilling (UVAN) method to fabricate nanochannels on a monocrystalline silicon surface. Their results indicate that material removal during UVAN can be divided into three stages and that the high-pressure release rate leads to the transformation of the Si-II phase into the amorphous phase (α-Si) and many atomic-scale defects consisting of stacking faults and dislocations. This study provides meaningful insight and reference for our study on AlN. However, the underlying mechanism of material removal behavior under ultrasonic vibration energy fields remains unclear. Existing simulation studies still focus on explaining the enhancement effects on the processing rate and quality observed during macro/microscale material removal processes, lacking quantitative characterization at the atomic removal level. Ultrasonic vibration acting on the processing interface may enhance the formation of the machined surface, providing new atomic-level insights for exploring the limits of material processing to achieve ideally smooth atomic-level surfaces.

In this work, we investigated the nanoscale-to-atomic-scale material removal behavior of single-crystal AlN during UVA-scratching through MD simulations. The effects of ultrasonic vibration on surface frictional properties, roughness, and subsurface lattice damage during AlN scratching were elucidated. The material removal mechanism during UVA-scratching was investigated at the atomic level by analyzing the structure, stress, and temperature fields. This work provides theoretical insights for developing UVA ultraprecision machining technology for hard-brittle materials.

2 Methods

2.1 MD simulation model and potential function

The MD simulation models for ordinary scratching and UVA-scratching of AlN are displayed in Fig. 1. This model was composed of an AlN (0001) workpiece with a size of 330 Å (*X*-axis) × 247.94 Å (*Y*-axis) ×150 Å (*Z*-axis) and a spherical diamond tip with a radius of 40 Å, consisting of 1,119,794 atoms in total. The directions of the *X*-, *Y*-, and *Z*-axes were along the $[1\bar{2}10]$, $[10\bar{1}0]$, and [0001] crystal orientations of single-crystal AlN, respectively. The $[\bar{1}2\bar{1}0]$ and $[000\bar{1}]$ directions were set as fixed boundary conditions, $[1\bar{2}10]$ and [0001] were set as shrink-wrapped boundary conditions, and $[10\bar{1}0]$ and $[\bar{1}010]$ were set as periodic boundary conditions. The AlN workpiece contained three layers, i.e., the boundary layer, the thermostat layer, and the Newtonian layer. The boundary layer with a thickness of 10 Å was used to fix the AlN workpiece to execute the scratching process. The Langevin thermostat bath method was adopted to maintain a constant thermostat layer temperature and dissipate the scratching-induced heat [42, 43]. The Newtonian layer with dimensions of 300 Å × 247.94 Å × 120 Å followed Newton's second law. Figure 1 shows that the motion of the tip was configured as a combination of elliptical vibrations in the *X*- and *Y*-directions and uniform linear feed motion in the *X*-direction during UVA-scratching. The motion equation can be described as Eqs. (1) and (2):

$$v_x(t) = A_x\cos(2\pi ft) + v_t \tag{1}$$

$$v_y(t) = A_y\sin(2\pi f) \tag{2}$$

where v_t is the scratching velocity along the *X*-direction, $v_x(t)$ is its velocity components along the *X*-direction at t, $v_y(t)$ is its velocity components along the *Y*-direction, t is the motion time of the tip, f is the ultrasonic vibration frequency, and A_x and A_y are the ultrasonic vibration amplitudes in the *X*- and *Y*-directions, respectively. In contrast, the tip moved uniformly in a straight line along the *X*-direction during scratching without vibration. The detailed simulation parameters are listed in Table 1. The Vashishta potential [44] function was used to describe the interatomic interactions within the AlN workpiece, as AlN does not easily react with diamonds under ordinary scratching conditions. The Lenard–Jones potential function was utilized to characterize the interaction of C–Al and C–N pairs between the diamond tip and the AlN workpiece [45].

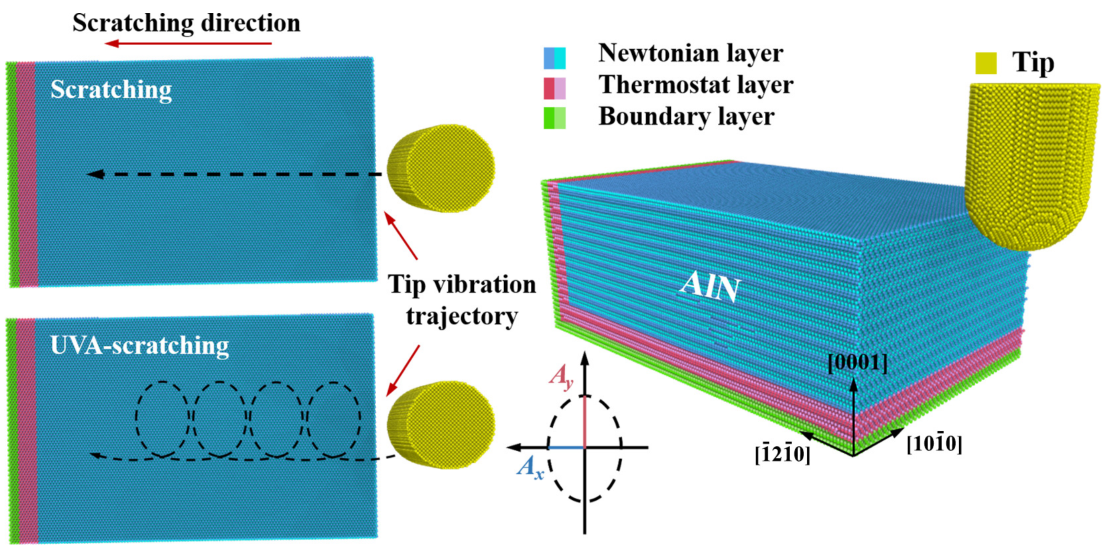

Fig. 1 MD simulation model for ordinary scratching and UVA-scratching of an AlN workpiece with a diamond tip.

Table 1 MD simulation parameters

Parameter	Value
Total number of atoms in AlN workpiece	1,051,836
Total number of atoms in diamond tip	67,958
Dimensions of the AlN workpiece (Å)	300 × 247.94 × 150
Radius of the diamond tip (Å)	40
Initial temperature (K)	300
Time step (fs)	1
Scratching distance, *L* (Å)	210
Scratch depth, *d* (Å)	10, 15, 20, 25, 30
Scratching velocity, *v* (Å/ps)	0.2, 0.4
Ultrasonic amplitude in *X*-direction, A_x (Å)	4
Ultrasonic amplitude in *Y*-direction, A_y (Å)	6
Ultrasonic vibration frequency, *f* (GHz)	0.25

2.2 Simulation and analytical methods

In this study, the Large-scale Atomic/Molecular Massively Parallel Simulator (LAMMPS, Version 12 Dec 2018) [46] was employed for all the MD simulations. Initially, the system was relaxed for 10 ps in a canonical (NVT) ensemble to ensure that it was sufficiently relaxed. Next, ordinary scratching and UVA-scratching simulations were performed in a microcanonical (NVE) ensemble. For analysis and postprocessing, OVITO software was used to capture multiple atomic snapshots and conduct in-depth data analysis [47]. The dislocation extraction algorithm (DXA) [48] and identify diamond structure (IDS) [49] methods were applied to identify atomic structure transformation during scratching and analyze subsurface dislocations and defects. Atomic displacement vectors and corresponding vector graphs showing the displacement trajectory of each atom were prepared to analyze the material deformation involving the plastic flow of AlN during scratching. Temperature and von Mises stress distribution maps were obtained to evaluate the effects of temperature and shear stress on the material removal behavior and subsurface damage during UVA-scratching and ordinary scratching. First, the von Mises stress and temperature of each atom were calculated according to the corresponding formula [50, 51]. Then, the whole Newtonian layer was divided into many unit spheres with a radius of 3.5 Å. Finally, the average von Mises stress and temperature in each sphere space were obtained, and the atoms belonging to a certain sphere were colored according to the calculated average value.

2.3 Nanowear experiments

Nanowear tests and three-dimensional (3D) imaging of the wear tracks were conducted by using an atomic force microscope (Dimension Edge, Bruker, Germany). The nanowear tests for the UVA and ordinary scratching modes were performed using a diamond tip with a nominal curvature radius of ~20 nm and a cantilever spring constant of ~100 N/m (NC-LC, Adama, USA) under a 1 μm scratching distance, at a 2 μm/s scratching velocity, and 50 reciprocating cycles at different normal forces in the range of 2.6–42.1 μN. The scratching direction was along the $[1\bar{2}10]$ crystal orientation. In the UVA-scratching process, ultrasonic vibration was applied perpendicular to the scratching direction with an amplitude of 10 nm and a frequency of 55 kHz. After scratching, the wear regions were scanned *in situ* using a sharp Si_3N_4 probe with a curvature radius of ~20 nm and a cantilever spring constant of ~0.1 N/m. An undoped single-crystal AlN (0001) film with a thickness of 3 μm on a 0.43-mm-thick sapphire substrate (Heifei Crystal Technical Material Co., Ltd., China) was used for our experiments. The surface root-mean-square (RMS) roughness of these AlN samples was measured to be less than 0.5 nm over an area of 6 μm × 6 μm using AFM.

3 Results and discussion

3.1 Scratching morphology and wear properties

The 3D topographies and cross-sectional profiles of the AlN workpiece at different scratching distances at scratch depths of 20 and 30 Å, as shown in Figs. 2 and 3, respectively, can reflect the evolution of surface material removal and structural characteristics in the subsurface during UVA-scratching and ordinary scratching. The slice thickness of these cross-sectional profiles is 40 Å, and atoms are colored according to their structural types identified using the IDS method. As the scratching distance increased, the surface pile-up and material removal volume increased, but the compression phase caused by the compressive stress of the tip gradually decreased. The final steady-state damage in the subsurface after unloading was primarily composed of stacking faults and dislocations. The cross-sectional profiles suggest that the AlN workpiece has fewer amorphous layers and stacking faults

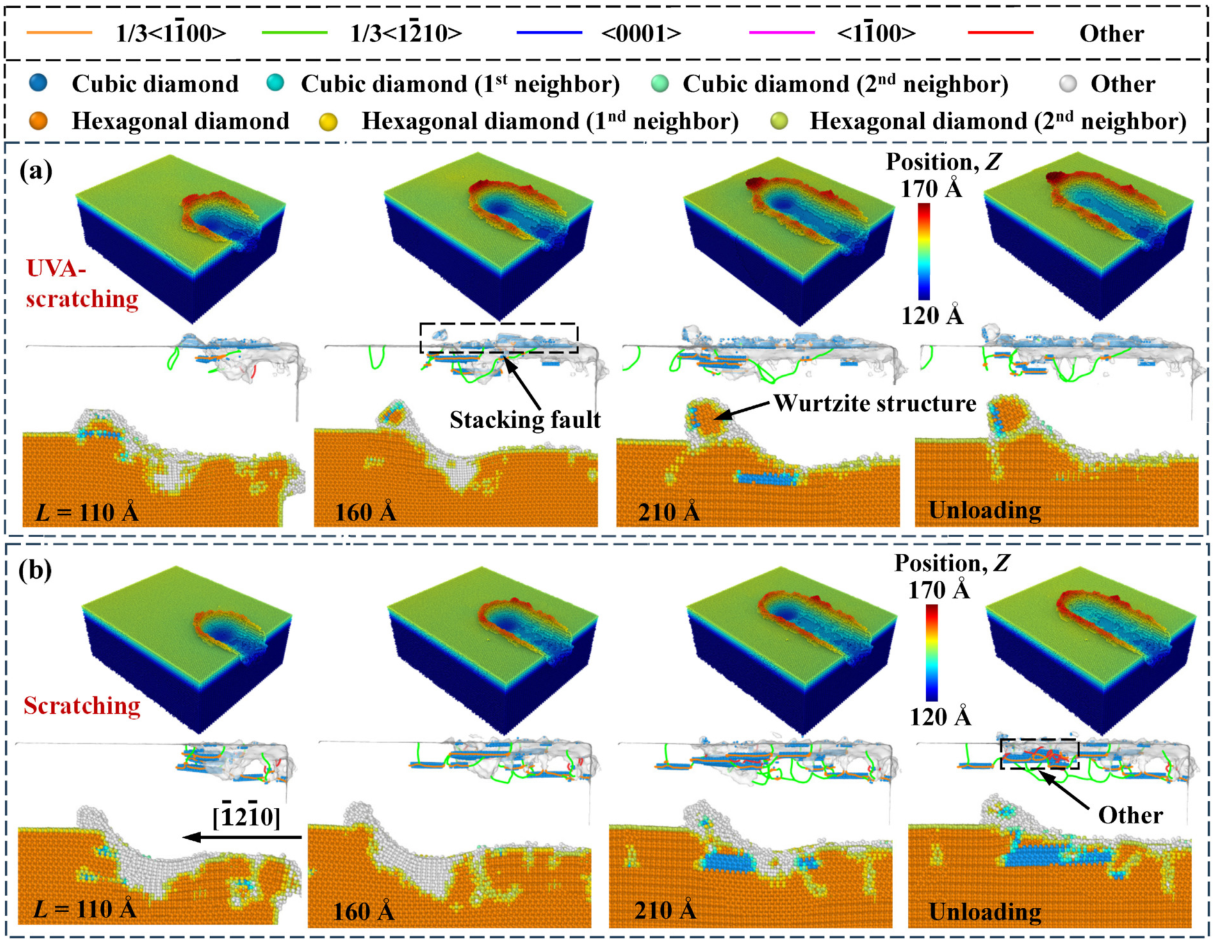

Fig. 2 Surface topographies and cross-sectional profiles of AlN workpiece when scratching distances L = 110, 160, and 210 Å and after unloading with a scratch depth d = 20 Å. (a) UVA-scratching; (b) ordinary scratching. Subsurface damage consisting of dislocations and structural transformation of AlN workpiece is also shown in this figure. Scratching velocity is 0.4 Å/ps.

after UVA-scratching than after ordinary scratching. UVA-scratching and ordinary scratching resulted in different structural features in the pile-up: UVA-scratching retained many atoms with the original wurtzite crystal structure, whereas ordinary scratching mostly produced an amorphous structure. This result indicates some differences in the material removal mode between UVA-scratching and ordinary scratching of AlN. The DXA analysis results indicate that at a scratching distance of L = 110 Å, fewer stacking faults appeared in the workpiece, with a shallower distribution after UVA-scratching than after ordinary scratching. For the 20 Å scratch depth, dislocations of an unknown type (marked in red) appeared when the scratching distance L = 160 Å, whereas dislocations of an unknown type appeared earlier in the scratching process with a 30 Å scratch depth. With increasing scratching distance, the stacking faults expanded in the surface layer of the AlN workpiece but did not extend and developed deeper for UVA-scratching. When the scratching distance L = 210 Å, the AlN workpiece after ordinary scratching exhibited an extensive distribution of stacking faults at both ends of the tip contact area. In contrast, the stacking faults caused by UVA-scratching were distributed mainly at the front of the tip contact area, with a narrow distribution range. Compared with that before unloading, the subsurface damage consisting of stacking faults and dislocations during ordinary scratching was not significantly reduced, whereas the subsurface damage caused by UVA-scratching was slightly alleviated. The 30 Å scratch depth resulted in more severe surface wear and pile-up, and the subsurface damage consisting of dislocations and stacking faults than the 20 Å scratch depth. After ordinary scratching, when the scratch depth reached 30 Å, the amorphous structure in the pile-up and debris was also mixed with the evident wurtzite and cubic diamond (CD) structures, and material removal at this time exhibited certain brittle fracture characteristics. Additionally, the morphology of the pile-up caused by UVA-scratching was quite different from that caused by ordinary scratching. Previous studies considered dislocation slip and stacking faults as the dominant mechanisms of material removal of AlN crystals [52] during single-point diamond abrasive scratching. The shallow and flake stacking faults expand laterally along the tip movement direction during UVA-scratching. Moreover, shallow surface stacking faults can release the internal stress of the material to some extent, thereby alleviating damage to the subsurface.

The atomic displacement and surface pile-up after unloading for UVA-scratching and ordinary scratching at a scratch depth of d = 30 Å are shown in Fig. 4. The plot of the atomic displacement vectors displays the displacement trajectory of each atom during scratching. For UVA-scratching, atoms in the scratching region flowed in many directions and moved to both sides of the scratched trench. In contrast to UVA-scratching, there was only one primary atomic movement direction for ordinary scratching (i.e., the [$\bar{1}2\bar{1}0$] crystal direction), along which there was a longer displacement distance. The 3D scratching topographies suggest that, after UVA-scratching, less surface pile-up formed than after ordinary scratching, as the tip only moved in the X-direction. This

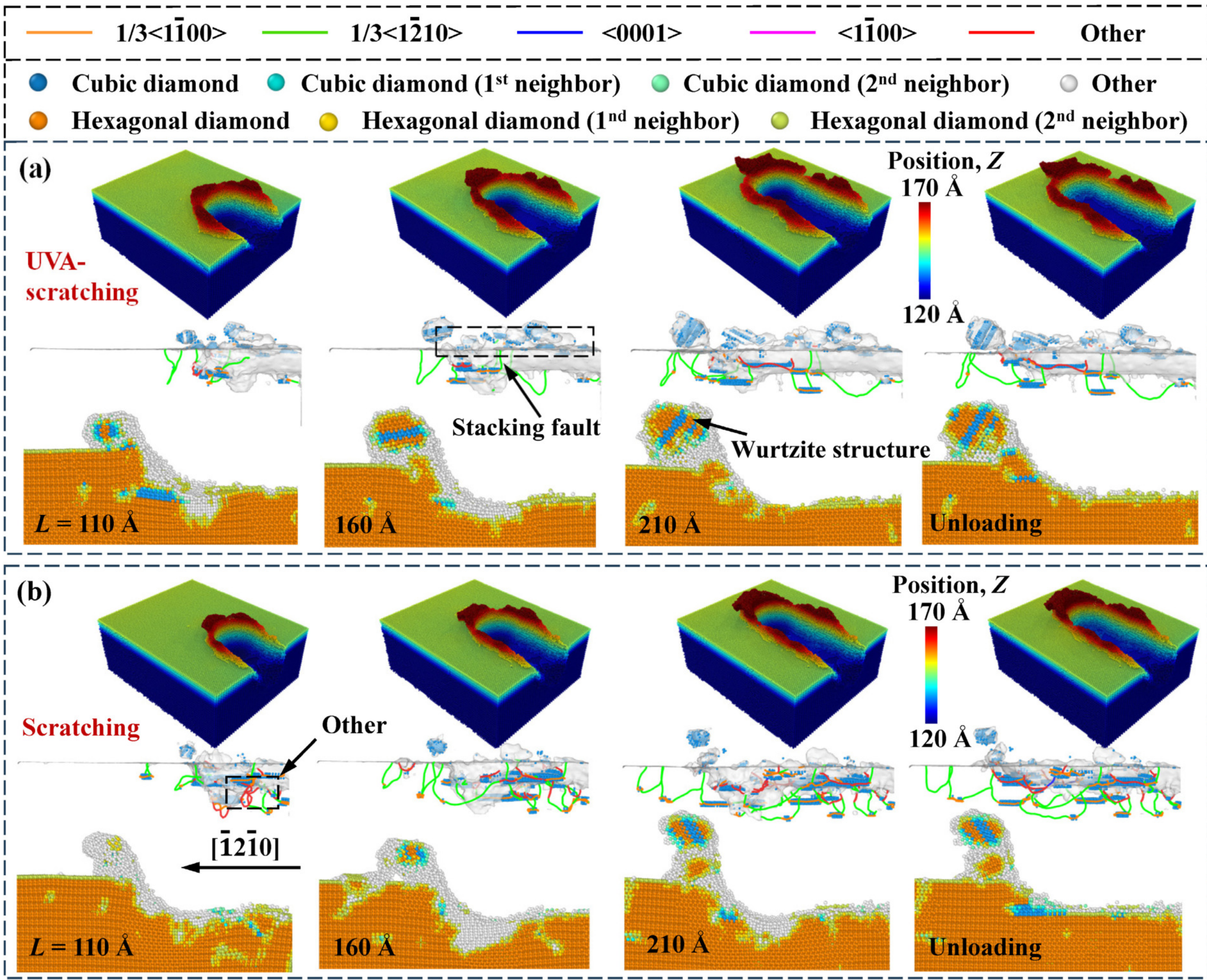

Fig. 3 Surface topographies and cross-sectional profiles of AlN workpiece when scratching distances L = 110, 160, and 210 Å and after unloading with a scratch depth d = 30 Å. (a) UVA-scratching; (b) ordinary scratching. Subsurface damage consisting of dislocations and structural transformation of AlN workpiece is also shown in this figure. Scratching velocity is 0.4 Å/ps.

caused the debris atoms to concentrate on the front and sides of the scratching trace. In the case of UVA-scratching, the debris atoms moved in the extra X- and Y-directions due to the tip vibration, which greatly reduced the pile-up in front of the tip-scratching trace. Distinguishing the structural characteristics of pile-up and debris can help understanding the material removal mechanism, which can be generally divided into plastic removal and brittle fracture modes for hard-brittle materials. The IDS method was used in this study to identify the lattice structure of pile-up and debris (Fig. 4). Compared with ordinary scratching, the pile-up and debris for UVA-scratching contained more evident CD structures transferred from the original hexagonal diamond (HD) structure of AlN. The CD structure here was presumed to be a zinc-blende structure that has higher symmetry than hexagonal wurtzite, overlapping positive and negative ion centers, and no spontaneous polarization [53, 54]. The amorphous state identified as "other" by the IDS method after UVA-scratching was also less than that after ordinary scratching.

The difference in the structural properties of pile-up and debris between UVA-scratching and ordinary scratching was attributed primarily to the coupling effect of the temperature and stress fields. Specifically, the local high temperature during UVA-scratching reduced the energy required to cause phase transitions from the wurtzite structure to the zinc-blende structure and other transient phases before finally becoming a zinc-blende structure. The contents concerning the temperature and stress fields are discussed in more detail in Section 3.3. For ordinary scratching, a slight increase in local temperature was insufficient to induce this phase transition, as it merely resulted in most of the wurtzite structure becoming amorphous instead.

Hard-brittle materials, such as AlN, GaN, and sapphire, have similar surface morphologies and wear properties during UVA-scratching. However, the surface morphology and local phase transformation of these materials during UVA-scratching also exhibited some differences, especially when the feature scale reached the nanoscale or the atomic scale. After UVA-scratching, more evident surface pile-up and debris consisting of many CD atoms occurred on the AlN workpiece due to local phase transitions, whereas some amorphous atoms were primarily distributed on the groove with a flatter scratched surface. This phenomenon suggests that the material removal behavior of AlN during UVA-scratching was not just attributed to plastic removal but was far more complicated than that during ordinary scratching. In contrast, the height of the material pile-up on sapphire after UVA-scratching is smaller, and the structures of the pile-up and debris are mostly amorphous because of extrusion and shearing [55]. Furthermore, although both AlN and GaN crystals have the same wurtzite structure, many differences exist in their material removal behaviors during UVA-scratching. For GaN, many amorphous atoms are generated in the pile-up and wear debris, and the subsurface damage is mainly composed of various dislocations, suggesting that the material removal of GaN during UVA-scratching might still be dominated by crystal plasticity [28, 56, 57].

We also performed another UVA-scratching and ordinary scratching simulation with a slower feed scratching velocity of 0.2 Å/ps and found that there was little difference in the scratching results between the two velocities. Notably, UVA-scratching and ordinary scratching have similar trends in terms of friction, wear, subsurface damage, etc., regardless of the selected scratching velocities. Most results for the 0.2 Å/ps scratching velocity are given in the Electronic Supplementary Material (ESM).

The wear volume and removal rate were calculated to quantify the material removal behavior for UVA-scratching and ordinary scratching under different mechanical conditions (Fig. 5). The wear volume was obtained by integrating the volume of the scratching-induced trench [58], and the removal rate was defined as the ratio of the number of atoms removed to the number of atoms theoretically removed in the trench. The calculation results revealed that UVA-scratching resulted in a greater wear volume and removal rate than ordinary scratching for all selected scratch depths and scratching velocities in our simulation. This result suggests that inducing vibration could effectively promote nanoscale material removal during mechanical scratching with a diamond tip. Figure 6 displays the wear volume as a function of the normal force for UVA-scratching and ordinary scratching. The wear volume of the AlN workpiece for UVA-scratching was larger than that for ordinary scratching at the same normal force.

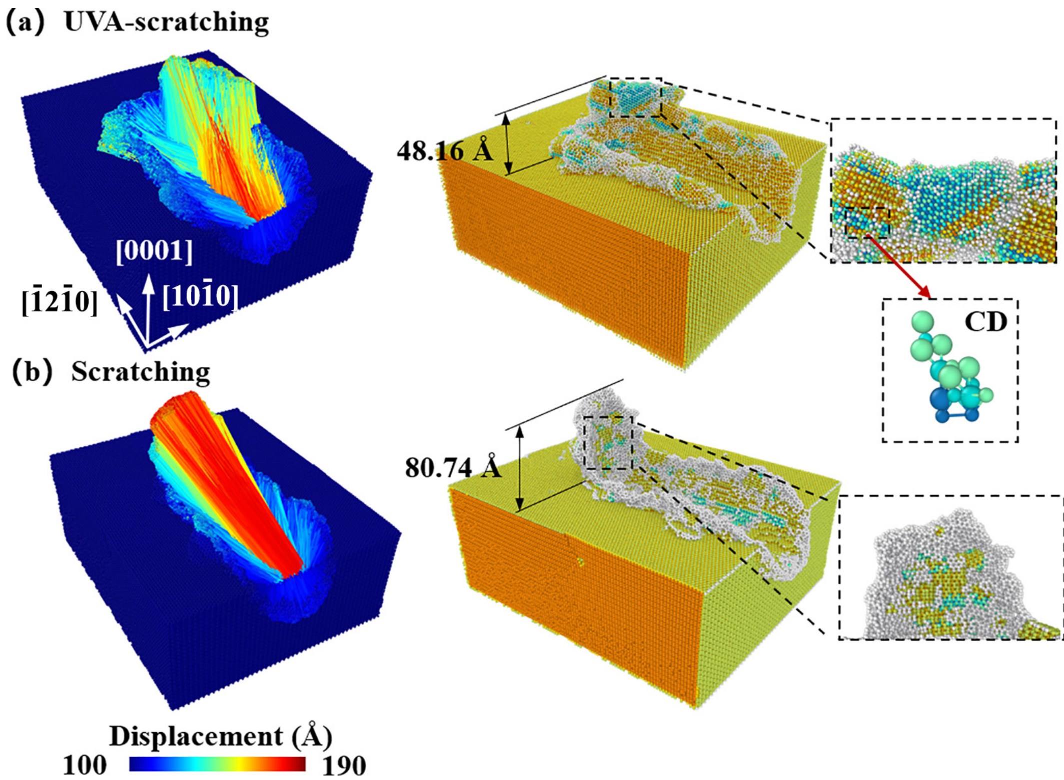

Fig. 4 Scratching-induced atomic displacement and surface pile-up. (a) UVA-scratching; (b) ordinary scratching. Scratch depth is 30 Å and scratching velocity is 0.4 Å/ps.

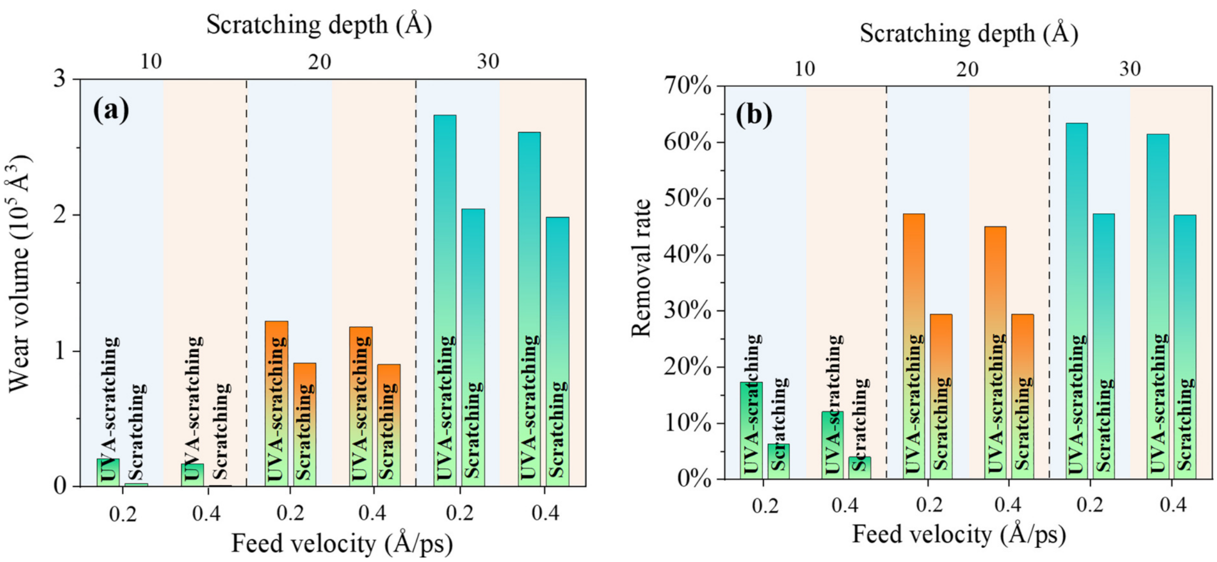

Fig. 5 (a) Wear volume and (b) removal rate of AlN workpiece after scratching under different conditions.

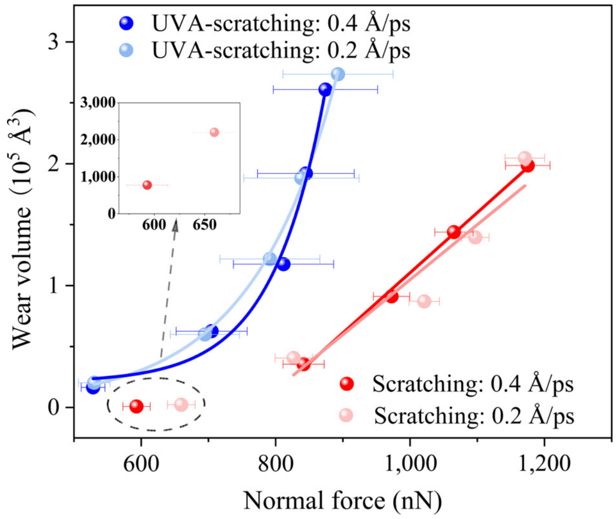

Fig. 6 Wear volume as a function of normal force in AlN workpiece for UVA-scratching and ordinary scratching.

As the normal force increased, the wear volume for UVA-scratching increased exponentially, and the greater the speed was, the faster the wear volume increased. The wear volume exhibited an approximately linear relationship with the normal force in the approximate range of 800–1,200 nN. The increase rate of wear volume against the normal force for UVA-scratching, which can reflect the wear rate, was considerably faster than that for ordinary scratching, indicating that UVA-scratching can achieve more efficient material removal under the same normal force conditions.

AFM-based nanoscale UVA-scratching and ordinary scratching experiments were performed on single-crystal AlN surfaces at different normal forces in the range of 2.63–42.08 μN using a diamond tip. Figure 7 displays the AFM images of the wear tracks and wear volume as a function of the normal force after scratching. When the normal force was 2.63 μN, evident wear occurred at a depth of ~8.6 nm after UVA-scratching, but only slight wear occurred on the AlN surface after ordinary scratching. This suggests that purely mechanical removal is difficult to achieve using ordinary scratching. Wear increased with increasing normal force for both UVA-scratching and ordinary scratching. Under the same normal force conditions, the wear volume for UVA-scratching was at least four times greater than that for ordinary scratching. Furthermore, the wear volume as a function of normal force for UVA-scratching demonstrated a noticeably different trend from that for ordinary scratching: an exponential increase for UVA-scratching but a linear increase for ordinary scratching that conformed to classic Archard theory. The above results indicate that the nanowear experiment exhibited a material removal phenomenon similar to that of the MD simulation for UVA-scratching and ordinary scratching.

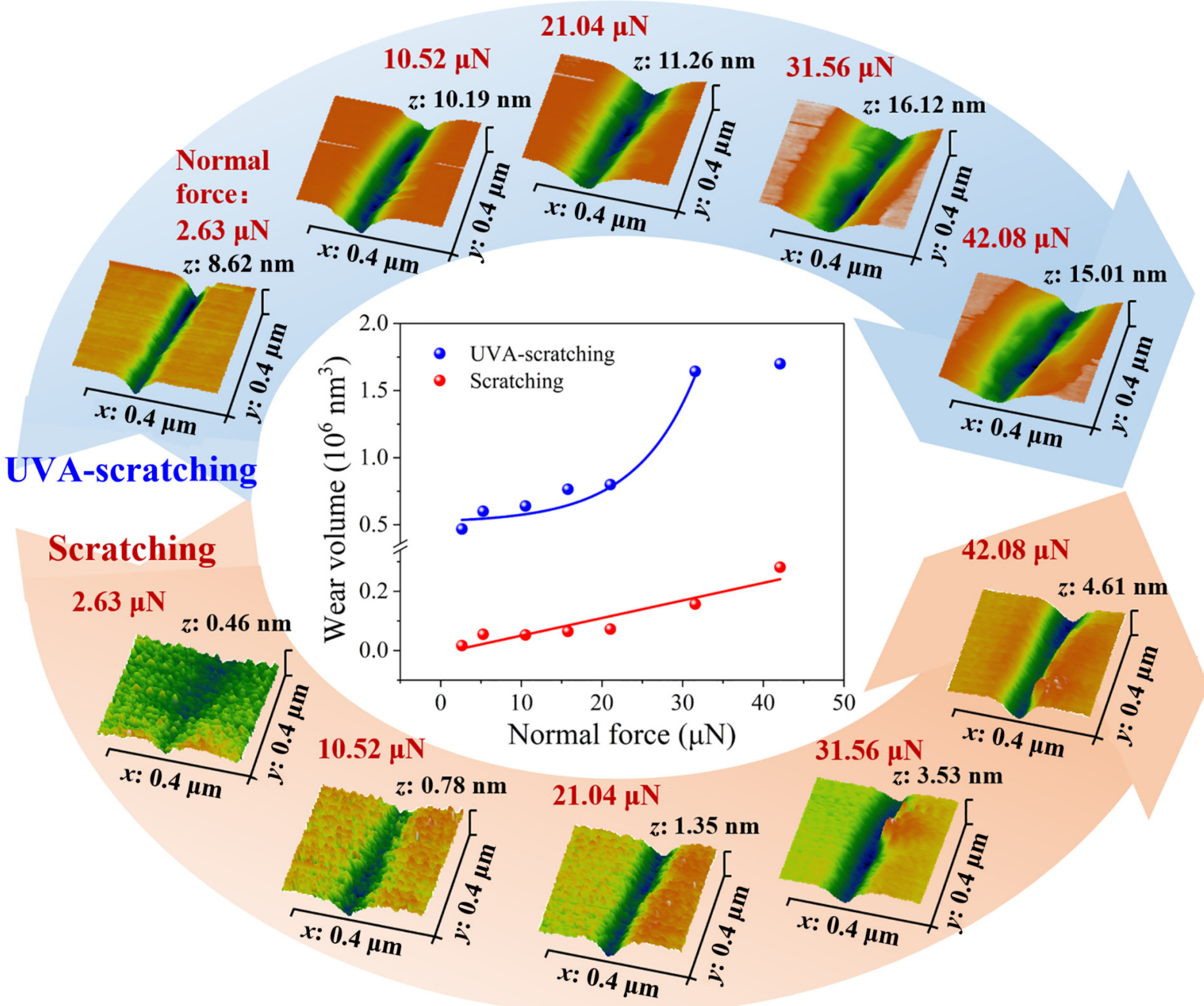

Fig. 7 AFM images of wear tracks at different normal forces and wear volumes as a function of normal force for UVA-scratching and ordinary scratching.

As roughness is an important index for evaluating the quality of ultraprecision surface processing, the RMS roughness values at different positions were measured. The surface morphologies shown in Figs. 8(a) and 8(b) indicate that the scratched surface after UVA-scratching is flatter than that after ordinary scratching at the same scratch depths of 20 and 30 Å, along with fewer pile-ups and more ordinary arrangements of surface atoms. The RMS values were measured at the center position of the scratching-induced trench after UVA-scratching and ordinary scratching. As shown in Figs. 8(c) and 8(d), the RMS values for UVA-scratching were all evidently lower than those for ordinary scratching at five different positions. The average RMS roughness after UVA-scratching (both lower than 0.4 Å) was approximately one-third that after ordinary scratching (Fig. 8(e)). The above results demonstrate that UVA-scratching can result in lower surface roughness than ordinary scratching, thereby improving surface machining quality.

Multiple abrasive particles and their interactions are usually involved in ultraprecision surface machining. Here, we performed an additional MD simulation of UVA-scratching and ordinary scratching with two diamond tips for the AlN workpiece. Similar to single-tip scratching, UVA-scratching and ordinary scratching with two tips resulted in differences in surface wear morphology, wear volume, and subsurface damage. During double-tip scratching, the scratching force generated by the two tips propagated continuously, and the atoms in the contact area were under forces from multiple directions, resulting in the dislocations extending deeper into the subsurface. This phenomenon may be related to the atoms obtaining excessive instantaneous energy during double-tip scratching. The surface pile-up produced after double-tip UVA-scratching contained the original wurtzite crystal structure, whereas that after double-tip ordinary scratching was mainly composed of an amorphous structure, suggesting a more evident plastic removal feature. Regardless of single-tip mode or double-tip mode, UVA-scratching always results in a flatter surface and much lower surface roughness than ordinary scratching. In addition, the surface morphology and RMS values of the two grooves induced by double-tip scratching exhibited individual variability. A detailed explanation of double-tip UVA-scratching is given in the ESM.

3.2 Frictional properties

Figure 9 shows the evolution of the tangential force (Figs. 9(a)–9(c)) and normal force (Figs. 9(d)–9(f)) during UVA-scratching and ordinary scratching at scratch depths of d = 10, 20, and 30 Å, in which the periodic fluctuating lines were smoothed as solid lines to reflect the instantaneous average force situation. As the scratching distance increased, the tangential force first increased rapidly and then gradually reached a steady state accompanied by oscillations within a certain range for both the UVA-scratching and ordinary scratching cases. For UVA-scratching, the tangential and normal forces oscillated periodically due to the periodic movement trajectory of the tip vibration, where the greater the scratch depth was, the greater the oscillation amplitude. The tangential and normal forces for UVA-scratching were smaller than those for ordinary scratching in the stabilizing scratching stage when the scratch depth was d = 20 or 30 Å. Figure 10 displays that, except in the case of the 10 Å scratch depth, UVA-scratching resulted in a lower average friction force and friction coefficient than ordinary scratching did in the stable scratching stage. This result indicated that the addition of ultrasonic vibration can reduce friction during nanoscale scratching of the diamond tip against AlN workpieces. This is because the tip velocity is the sum of the speeds in the X-direction feed, X-direction vibration, and Y-direction vibration in the UVA-scratching process, resulting in a faster instantaneous velocity than ordinary scratching, thereby reducing the instantaneous contact area between the diamond tip and the AlN workpiece. Moreover, the force magnitude is determined by the instantaneous contact area; that is, both the tangential and normal forces increase with increasing contact area [59, 60]. Conversely, a decrease in the instantaneous contact area results in a reduction in the force for

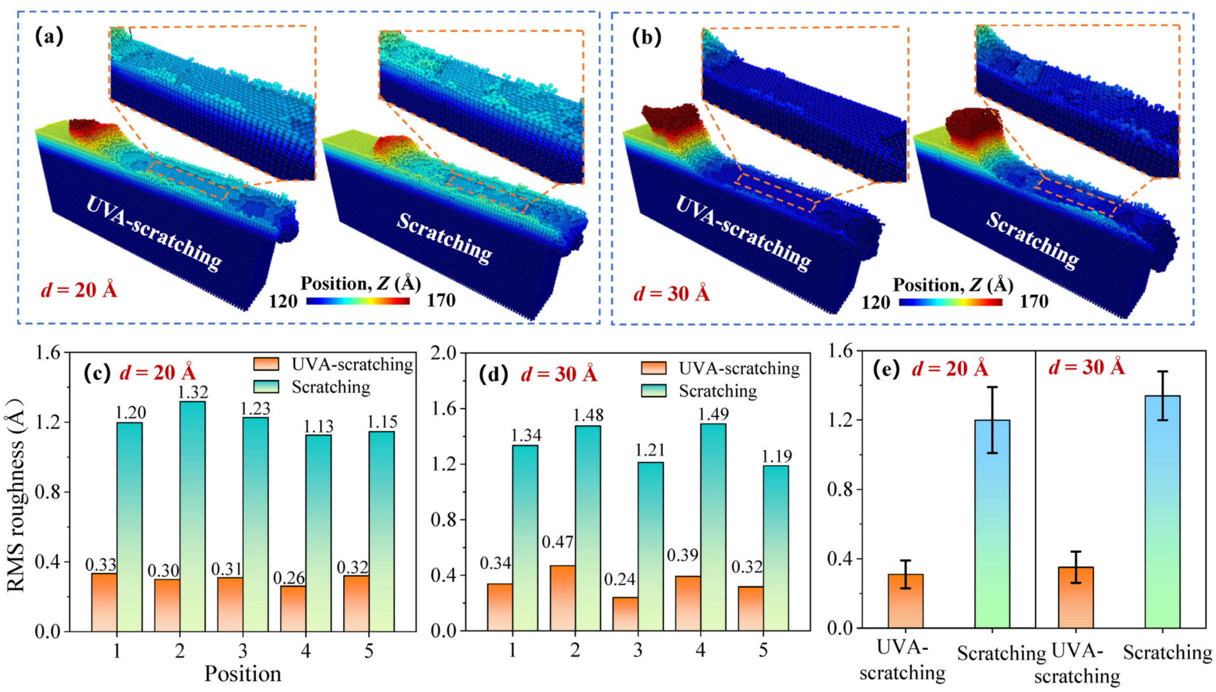

Fig. 8 Morphology and roughness of scratched surface of AlN workpiece: Comparison of surface morphology for UVA-scratching and ordinary scratching: (a) d = 20 Å; (b) d = 30 Å. RMS roughness values at five different positions in center of scratched region: (c) d = 20 Å; (d) d = 30 Å. (e) Average RMS roughness values for UVA-scratching and ordinary scratching at scratch depths of d = 20 and 30 Å. Scratching velocity is 0.4 Å/ps.

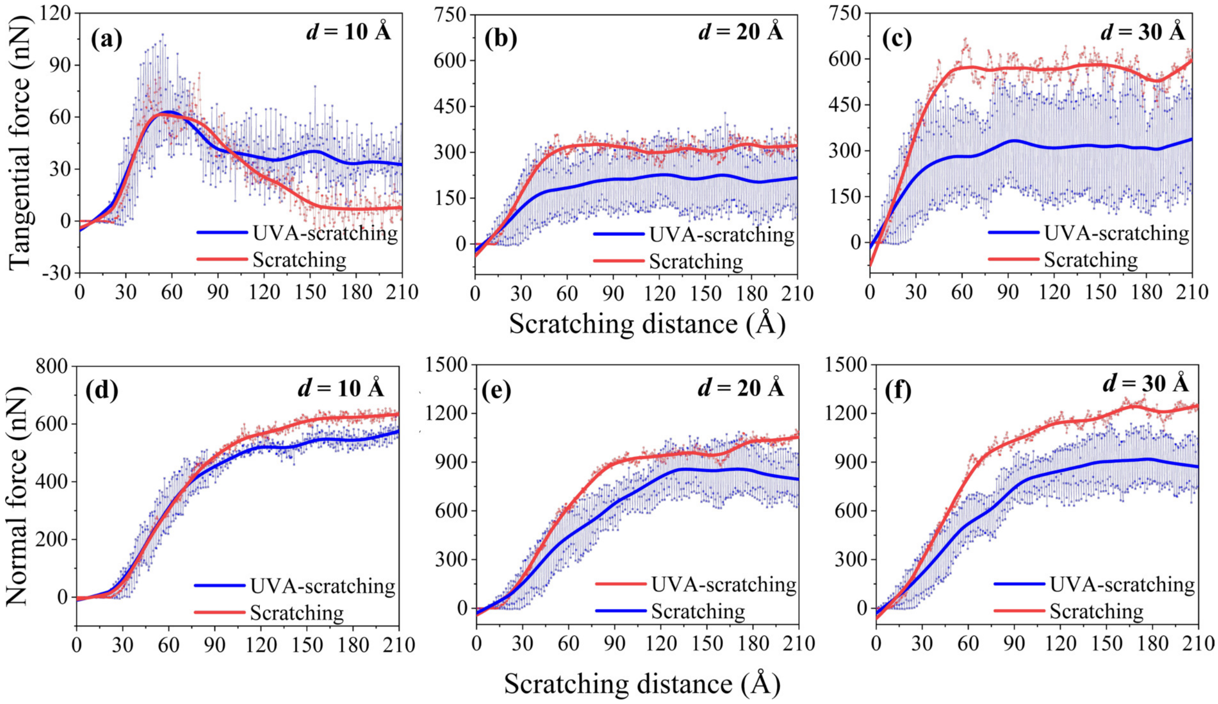

Fig. 9 Evolutions of (a–c) tangential force and (d–f) normal force during scratching for UVA-scratching and ordinary scratching at different scratch depths of d = 10, 20, and 30 Å. Scratching velocity is 0.4 Å/ps.

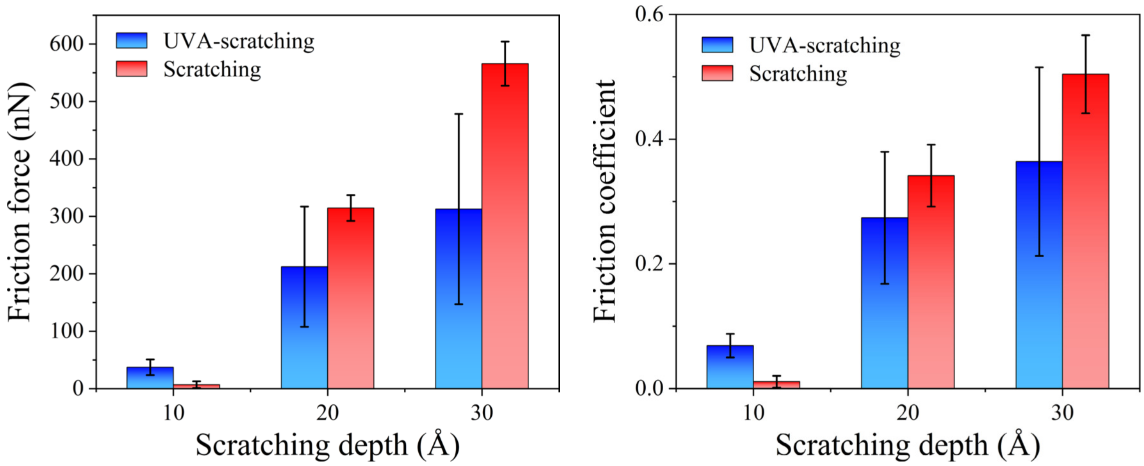

Fig. 10 Friction force and friction coefficient for UVA-scratching and ordinary scratching at different scratch depths of d = 10, 20, and 30 Å. Scratching velocity is 0.4 Å/ps.

UVA-scratching. Since the instantaneous contact area between the tip and the AlN workpiece changes with the vibration trajectory during UVA-scratching, both the tangential and normal forces fluctuate periodically with the vibration trajectory of the tip. Moreover, wear debris accumulates continuously with increasing scratching distance to form surface pile-ups. This pile-up formation increased the overall contact area between the tip and the AlN workpiece, resulting in a sustained increase in the tangential and normal forces [61]. When the scratch depth was 10 Å, UVA-scratching resulted in greater tangential force than ordinary scratching did at the scratching distance range of 120–210 Å because of the greater degree of material removal in the former (Fig. 16).

3.3 Stress and temperature distributions

High local stress increases the likelihood of material damage, which affects the quality of surface processing [62]. To evaluate the local stress field and its influence on the scratching-induced subsurface damage properties during UVA-scratching, the von Mises stress per atom was calculated, and then the stress distribution was further plotted against the average stress value within a certain volume range [63]. Figures 11(a) and 11(b) show the von Mises stress distributions of the AlN workpieces for scratch depths of 10, 20, and 30 Å when the scratching distance L = 210 Å and after tip withdrawal for UVA-scratching and ordinary scratching, respectively. UVA-scratching produced a narrower von Mises stress field, and its region of high stress was less evident than that of ordinary scratching. The above results suggest that introducing vibration could significantly reduce the region of local stress concentration within the AlN workpiece. In contrast, the region of localized stress concentration after scratching was larger and extended deeper along the movement direction of the tip. For both UVA-scratching and ordinary scratching, the local stress recovered partially after the tip was withdrawn and then manifested as residual stress. This residual stress might cause the further development of dislocations and even crack formation, thereby affecting the machining quality of the target workpiece [64]. Since the UVA-scratching case shows more elastic-dominated stress recovery and less residual stress distribution in the AlN workpiece, it is more suitable for obtaining low machining damage.

Given that temperature has an evident influence on material removal, high temperature is considered a potentially effective means to improve the machinability of hard-brittle materials [65–67]. Thus, understanding the effects of temperature on material removal and subsurface damage during UVA-scratching is highly important. The temperature cloud map shown in Figs. 12(a)–12(c) reveals that UVA-scratching exhibited evident localization in the high-temperature zone in the tip-workpiece contact region, whereas ordinary scratching did not. This phenomenon was also

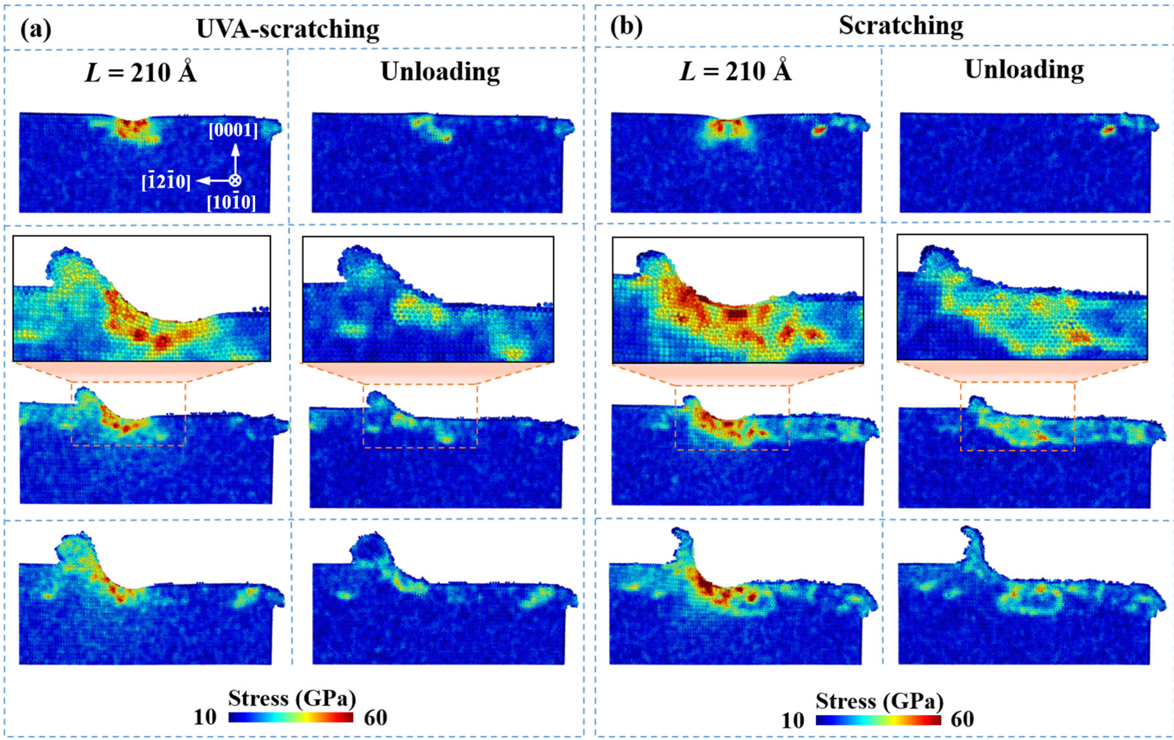

Fig. 11 Von Mises stress distribution when scratching distance $L = 210$ Å and after unloading for different scratch depths of $d = 10$, 20, and 30 Å. (a) UVA-scratching; (b) ordinary scratching. Scratching velocity is 0.4 Å/ps.

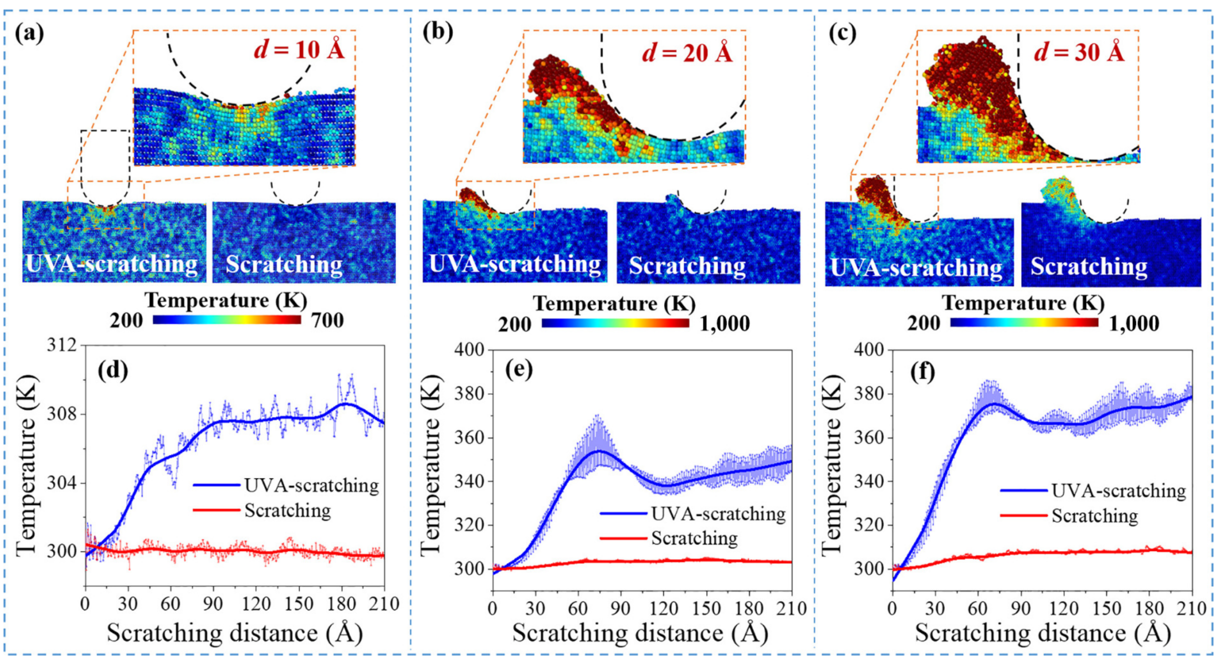

Fig. 12 Temperature distributions in tip-workpiece contact region for UVA-scratching and ordinary scratching at different scratch depths of (a) $d = 10$ Å, (b) $d = 20$ Å, and (c) $d = 30$ Å and the evolution of temperature during scratching for UVA-scratching and ordinary scratching for various scratch depths of (d) $d = 10$ Å. (e) $d = 20$ Å, and (f) $d = 30$ Å. Scratching velocity is 0.4 Å/ps.

confirmed in some MD studies on ultrasonic UVA-scratching [33, 68]. As the scratch depth increased, the range of the localized high-temperature region expanded. The temperature evolutions of the AlN workpiece during the scratching process for UVA-scratching and ordinary scratching at scratch depths of 10, 20, and 30 Å are shown in Figs. 12(d)–12(f), respectively. For ordinary scratching, the temperature was maintained around the initial temperature of 300 K throughout the entire scratching process, regardless of the scratch depth, suggesting that the scratching-induced heat dissipated over time. In contrast, UVA-scratching caused an evident increase in the temperature of the AlN workpiece, with the temperature increasing with increasing scratch depth. For UVA-scratching, the temperature at scratch depths of 20 and 30 Å first increased rapidly, then decreased, and continued to increase slowly. When the tip entered the edge of the workpiece, the contact area between the tip and the workpiece increased as the tip advanced, and the scratching-induced heat continued to increase, thereby increasing the statistical temperature of the AlN workpiece. After the tip completely penetrated the workpiece, the heat generated within a certain time tended to be stable. The heat dissipated was greater than the heat generated, resulting in a decrease in temperature. Finally, the slow increase in temperature was due to the continuous formation of pile-up, which caused some obstruction to temperature dissipation. Owing to the shallow tip penetration depth and minimal change in the contact area, the above phenomena did not occur at the 10 Å scratch depth. The occurrence of local high-temperature zones for UVA-scratching was due to the contact of the diamond tip with the surface atoms of AlN. This contact involved a combination of *X*-direction feed and *X*- and *Y*-direction vibrations, leading the atoms to acquire high instantaneous energy and thus generating high-temperature zones locally at the contact area. Owing to the more intense thermal activity of atoms, atomic bonds in these high-temperature zones could be broken more easily, and hence, material removal could be facilitated.

3.4 Subsurface damage

A previous study demonstrated that scratching-induced damage in the subsurface primarily consists of dislocations, stacking faults, structural transitions, and amorphizations [32]. Figure 13 displays the dislocation evolution of the AlN workpiece with four snapshots of the dislocation pattern at different times and the variations in the length of the dislocation lines with the scratching distance during UVA-scratching and ordinary scratching. The length of the dislocation lines increased as the nucleation and development of dislocations continued with increasing scratching distance. The range of dislocation distribution for UVA-scratching was smaller than that for ordinary scratching. During UVA-scratching, the length of the dislocation lines in the AlN workpiece fluctuated periodically, first increasing but then decreasing in one fluctuation cycle. In contrast, the length of the dislocation lines during ordinary scratching generally tended to increase. The length of the dislocation lines in both UVA-scratching and ordinary scratching decreased in the unloading stage, but the decrease in UVA-scratching was more pronounced. Figure 14 shows that ultrasonic vibration can effectively reduce subsurface damage, mainly in the form of fewer dislocations and stacking faults. The dislocation distribution was also shallower and more concentrated, with stacking faults located mainly in the shallower regions of the workpiece.

The statistics of the length of the dislocation lines with different Burgers vectors for different conditions are given in Fig. 15. Dislocations with Burgers vectors of 1/3 <$11\bar{2}0$> and 1/3 <$\bar{1}100$> and dislocations of unknown type constituted the vast majority, whereas a few dislocations had Burgers vectors of <$1\bar{1}00$> and <0001>. The length of each type of dislocation line for UVA-scratching is smaller than that for ordinary scratching. With respect to the effect of the scratch depth, the length of the dislocation lines increased as the scratch depth increased. Furthermore, slower feed rates led to a reduction in the length of the dislocation lines. The above results indicated that UVA-scratching generated fewer dislocations and stacking faults than

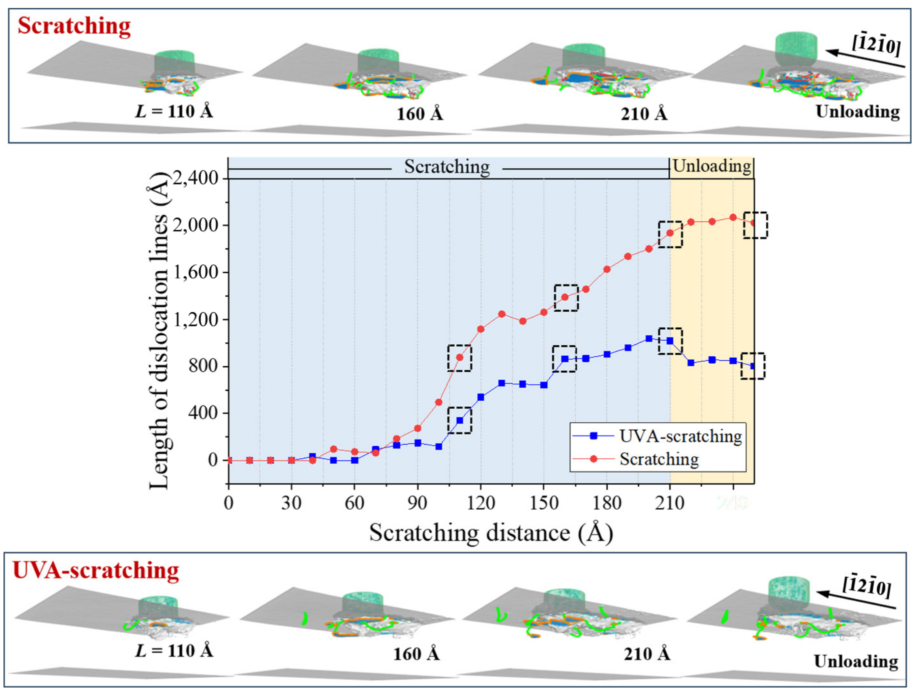

Fig. 13 Evolution of scratching-induced dislocations of AlN workpiece during UVA-scratching and ordinary scratching. Scratching velocity is 0.4 Å/ps.

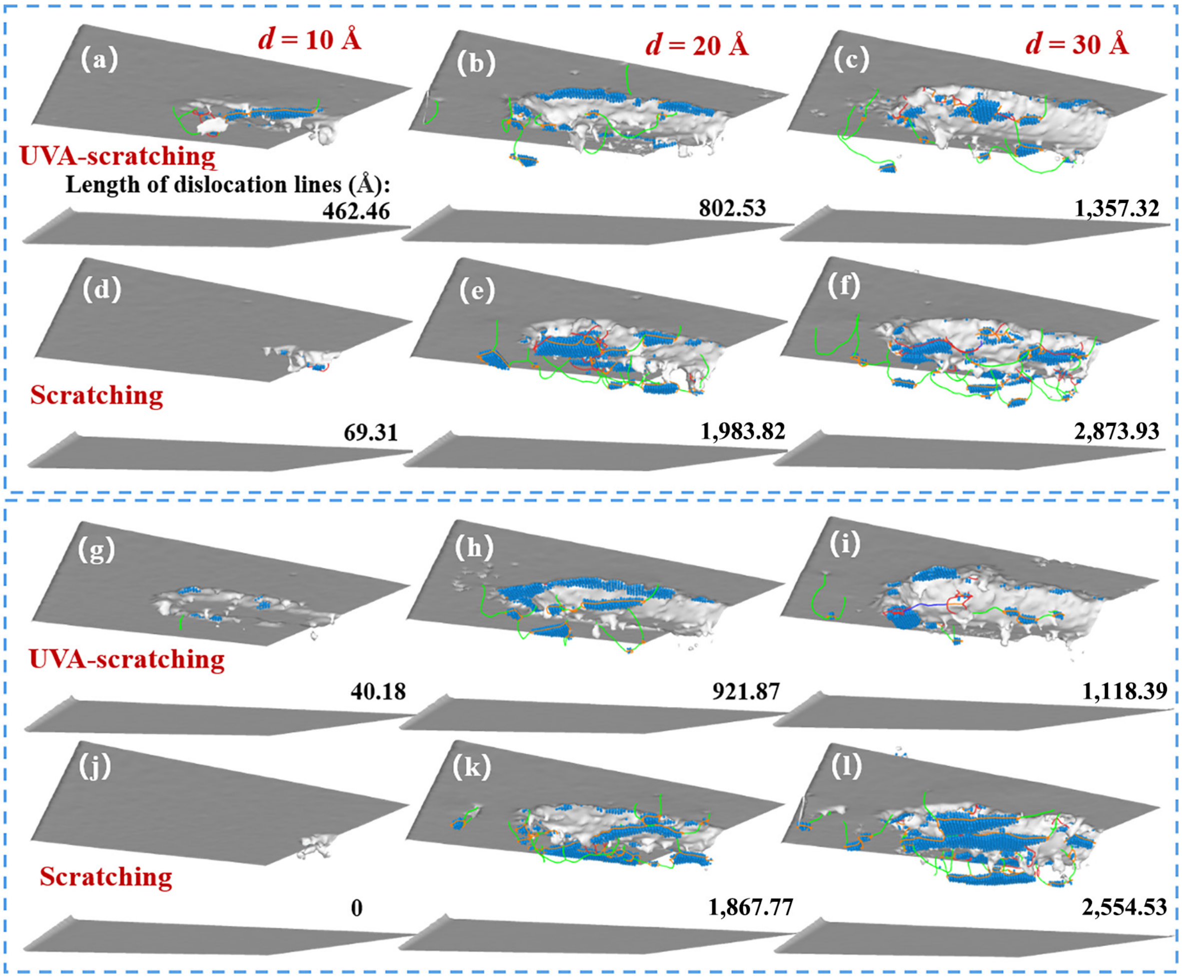

Fig. 14 Subsurface damage after UVA-scratching and ordinary scratching under different scratching conditions.

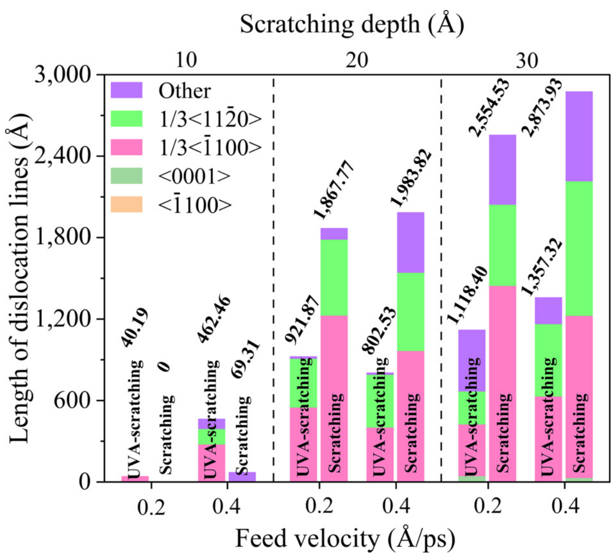

Fig. 15 Lengths of dislocation lines under different scratching conditions.

ordinary scratching, which can alleviate the degree of subsurface damage to a certain extent. Owing to the coupling of the stress and temperature fields, the AlN crystal undergoes a structural transition from HD to CD and an amorphous state. Because increasing the temperature could weaken the Al–N bond energy, the AlN workpiece with evident localized high-temperature zones after UVA-scratching is more likely to undergo phase transition (Fig. 4). In addition, the CD atoms were accompanied by the formation of a stacking fault. Figure 16 shows the statistical results of CD and "other" atoms after UVA-scratching and ordinary scratching at different feed velocities and scratch depths. Compared with ordinary scratching, UVA-scratching formed substantially fewer CD atoms and fewer "other" atoms, except at a scratch depth of d = 10 Å, indicating that adding ultrasonic vibration can reduce the phase transition from the HD to the CD structure and amorphization. The UVA-scratching strategy has advantages in preventing subsurface damage while ensuring effective material removal.

3.5 Monolayer removal

Understanding the material removal mechanism and its threshold condition with a single atom or molecule layer is highly important for the ultraprecision machining of hard-brittle semiconductor materials [69, 70]. When the scratch depth was 10 Å, monolayer removal of AlN occurred during both UVA-scratching and ordinary scratching, but the surface wear patterns of the two were significantly different (Fig. 17). For UVA-scratching, the uniform monolayer AlN was removed along the entire scratching trace, and a slight pile-up formed in front of the tip. A previous study showed that this monolayer removal situation is related to dislocation nucleation, which is thought to be the onset of plasticity in the AlN crystal [71]. In contrast, for the ordinary scratching case, only slight wear occurred at the starting position of scratching. More severe material removal corresponded with a greater tangential force for UVA-scratching. The tangential force

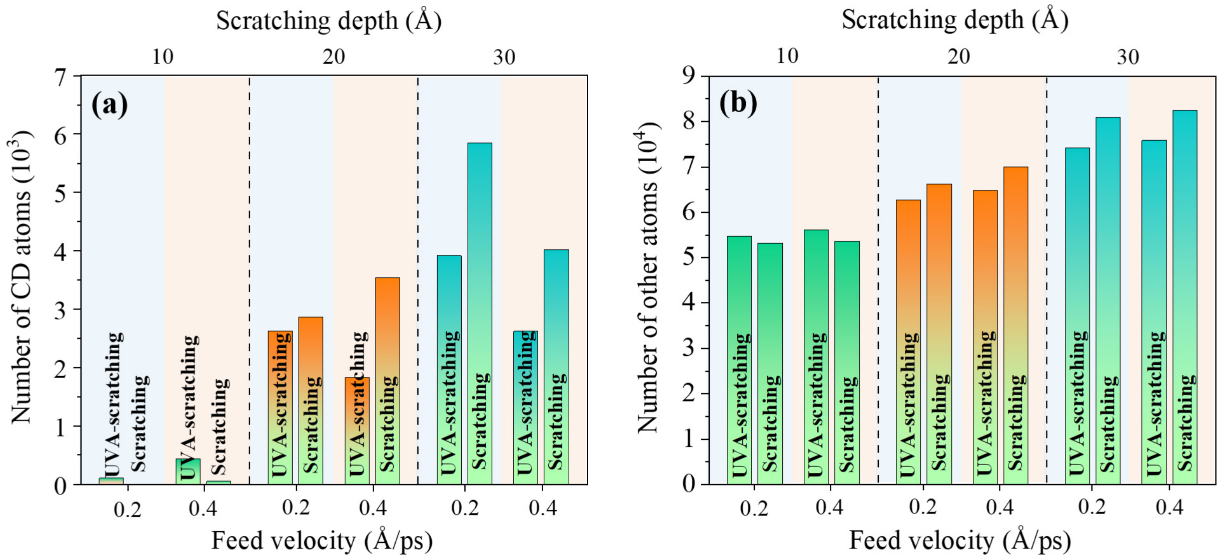

Fig. 16 Numbers of (a) CD atoms and (b) "other" atoms in AlN workpiece after scratching under different conditions.

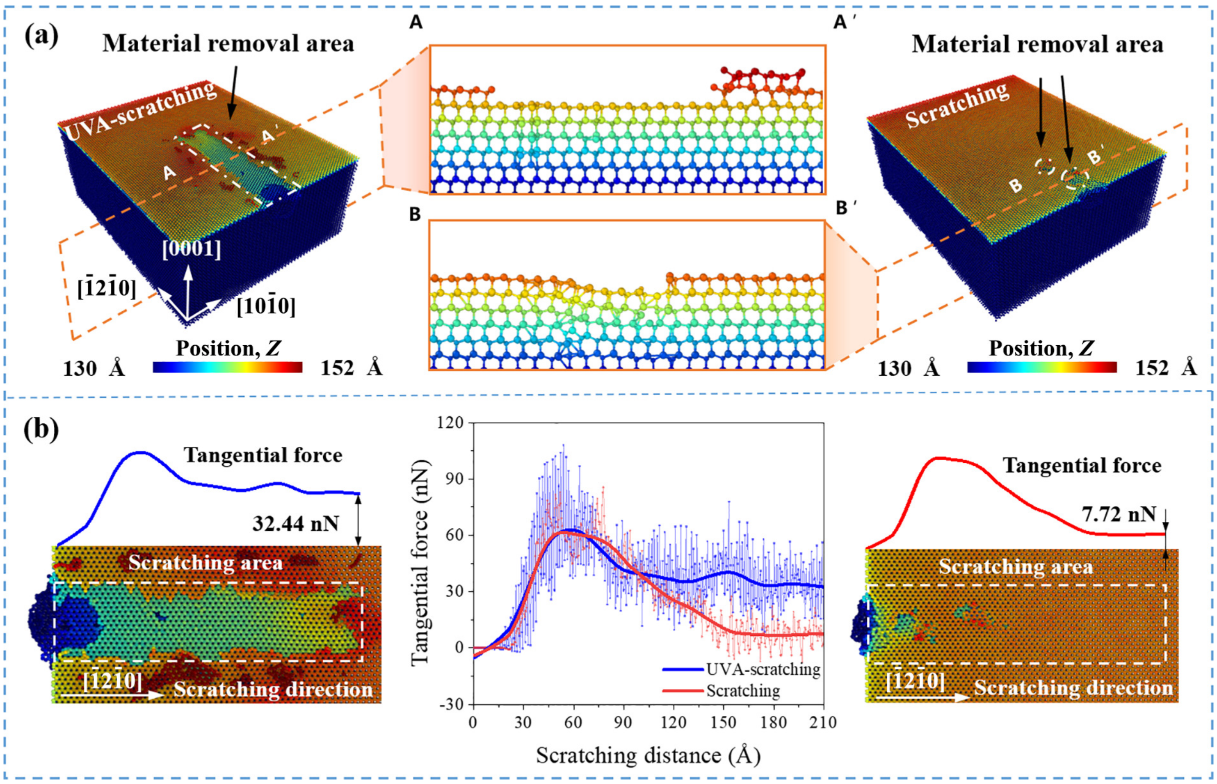

Fig. 17 Monolayer removal of AlN after UVA-scratching and ordinary scratching at the same scratch depth of 10 Å. (a) Wear morphology. (b) Tangential force along corresponding wear track. Scratching distance is 210 Å and scratching velocity is 0.4 Å/ps.

evolved through several stages: (I) The diamond tip began to scratch the AlN workpiece, and the tangential force gradually increased, leading to the removal of some atoms in the contact area. The tangential force in this stage was approximately the same for UVA-scratching and ordinary scratching. (II) The tangential force decreased until the steady state was reached. (III) In the steady state, the tangential force for UVA-scratching was greater than that for ordinary scratching, which resulted in stable monolayer removal without evident subsurface damage instead of slight lattice distortion. We speculate that the localized high-temperature zone in UVA-scratching is conducive to achieving monolayer removal of AlN crystals on the basis of the previous analysis concerning the temperature field. More studies on the monolayer removal behavior and the dependence of various parameters during UVA-scratching are needed in the future.

4 Conclusions

In this work, we primarily used MD simulations to investigate nanoscale-to-atomic-scale material removal and subsurface damage during UVA-scratching of monocrystalline AlN. UVA-scratching results in a lower tangential force, normal force, and friction coefficient than ordinary scratching because of the smaller instantaneous contact area between the diamond tip and the AlN workpiece. Inducing ultrasonic vibration can reduce the stress distribution range and restrain the stress concentration to a certain extent during scratching. In contrast, the local stress concentration during ordinary scratching becomes more pronounced and becomes worse as the scratch depth increases. Both the simulation and experimental results demonstrate that UVA-scratching results in a greater material removal volume and removal rate than ordinary scratching under the present conditions, primarily because the vibration-induced rise in local temperature facilitates atomic bond breakage and the lateral extension of stacking faults in the superficial layer. Compared with ordinary scratching, monolayer removal of AlN was easier to achieve by UVA-scratching, corresponding to an evident increase in the tangential force and friction coefficient. In both single-tip mode and double-tip mode, UVA-scratching always results in a much smoother surface than ordinary scratching does, with an RMS roughness lower than 0.4 Å. Furthermore, ultrasonic vibration can reduce scratching-induced material pile-up and subsurface damage, which mainly consists of dislocations and stacking faults.

Acknowledgements

This work was financially supported by the National Natural Science Foundation of China (Nos. 52405217 and 52475195), the Scientific Research Foundation of the University of South China, the Tribology Science Fund of the State Key Laboratory of Tribology in Advanced Equipment (No. SKLTKF24B08), and the University of South China Innovation Foundation For Postgraduate (No. 243YXC019). We would like to acknowledge the HPC Center of the University of South China for running the LAMMPS software.

Declaration of competing interest

The authors have no competing interests to declare that are relevant to the content of this article. The author Linmao Qian is the Editorial Board member of this journal.

Electronic Supplementary Material

Supplementary material is available in the online version of this article at https://doi.org/10.26599/FRICT.2025.9441097.

References

[1] Zhang S J, Zhou Y P, Zhang H J, Xiong Z W, To S. Advances in ultra-precision machining of micro-structured functional surfaces and their typical applications. *Int J Mach Tool Manu* **142**: 16–41 (2019)

[2] Hatefi S, Abou-El-Hossein K. Review of non-conventional technologies for assisting ultra-precision single-point diamond turning. *Int J Adv Manuf Tech* **111**(9–10): 2667–2685 (2020)

[3] Wang S, Zhao Q L, Yang X D. Surface and subsurface microscopic characteristics in sapphire ultra-precision grinding. *Tribol Int* **174**: 107710 (2022)

[4] Gu P, Zhang H H, You Z C, Shi Z Q. Surface roughness prediction of magnesium aluminum spinel in single-point oblique axis ultra-precision grinding. *Ceram Int* **50**(8): 13125–13136 (2024)

[5] Nasim M, Li Y C, Wen C E. Individual layer thickness-dependent nanoindentation and nanotribological behaviors of Ta/Co nanolaminates. *Tribol Int* **156**: 106845 (2021)

[6] Guo J, Gao J, Xiao C, Chen L, Qian L M. Mechanochemical reactions of GaN–Al_2O_3 interface at the nanoasperity contact: Roles of crystallographic polarity and ambient humidity. *Friction* **10**(7): 1005–1018 (2022)

[7] Hatefi S, Abou-El-Hossein K. Review of single-point diamond turning process in terms of ultra-precision optical surface roughness. *Int J Adv Manuf Tech* **106**(5–6): 2167–2187 (2020)

[8] Albisetti E, Calò A, Zanut A, Zheng X R, de Peppo G M, Riedo E. Thermal scanning probe lithography. *Nat Rev Method Prime* **2**: 32 (2022)

[9] Zhao G Y, Wei Z, Wang W L, Feng D H, Xu A X, Liu W L, Song Z T. Review on modeling and application of chemical mechanical polishing. *Nanotechnol Rev* **9**(1): 182–189 (2020)

[10] Brinksmeier E, Mutlugünes Y, Klocke F, Aurich J C, Shore P, Ohmori H. Ultra-precision grinding. *CIRP Ann—Manuf Techn* **59**(2): 652–671 (2010)

[11] Wojciechowski S, Krajewska-Śpiewak J, Maruda R W, Krolczyk G M, Nieslony P, Wieczorowski M, Gawlik J. Study on ploughing phenomena in tool flank face–workpiece interface including tool wear effect during ball-end milling. *Tribol Int* **181**: 108313 (2023)

[12] Meng Y G, Xu J, Jin Z M, Prakash B, Hu Y Z. A review of recent advances in tribology. *Friction* **8**(2): 221–300 (2020)

[13] Gao S, Lang H Y, Wang H X, Guo X G, Kang R K. Atomic understanding of elastic-plastic deformation and crack evolution for single crystal AlN during nanoscratch. *Ceram Int* **49**(22): 35357–35367 (2023)

[14] Zagorac D, Zagorac J, Djukic M B, Jordanov D, Matović B. Theoretical study of AlN mechanical behaviour under high pressure regime. *Theor Appl Fract Mec* **103**: 102289 (2019)

[15] Frentrup M, Lee L Y, Sahonta S L, Kappers M J, Massabuau F, Gupta P, Oliver R A, Humphreys C J, Wallis D J. X-ray diffraction analysis of cubic zincblende III-nitrides. *J Phys D Appl Phys* **50**(43): 433002 (2017)

[16] Lee K, Page R, Protasenko V, Schowalter L J, Toita M, Xing H G, Jena D. MBE growth and donor doping of coherent ultrawide bandgap AlGaN alloy layers on single-crystal AlN substrates. *Appl Phys Lett* **118**(9): 092101 (2021)

[17] Singhal J, Encomendero J, Cho Y, van Deurzen L, Zhang Z X, Nomoto K, Toita M, Xing H G, Jena D. Molecular beam homoepitaxy of N-polar AlN on bulk AlN substrates. *AIP Adv* **12**(9): 095314 (2022)

[18] Li Y F, Hu X T, Song Y M, Su Z L, Wang W Q, Jia H Q, Wang W X, Jiang Y, Chen H. The role of AlN thickness in MOCVD growth of N-polar GaN. *J Alloy Compd* **884**: 161134 (2021)

[19] Huang D, Liu Z, Harris J, Diao X G, Liu G H. High thermal conductive AlN substrate for heat dissipation in high-power LEDs. *Ceram Int* **45**(1): 1412–1415 (2019)

[20] König T, Burek B, Galetz M C. Effect of crystal orientation of AlN coatings on its high temperature oxidation in wet air. *J Eur Ceram Soc* **44**(2): 841–849 (2024)

[21] Zhang J G, Zheng Z D, Huang K, Lin C T, Huang W Q, Chen X, Xiao J F, Xu J F. Field-assisted machining of difficult-to-machine materials. *Int J Extreme Manuf* **6**(3): 032002 (2024)

[22] Guo Y J, Yang X J, Kang J, Li M Z, Xie Q M, Xiao J G, Zhang W Q. Experimental investigations on the laser-assisted machining of single crystal Si for optimal machining. *Opt Laser Technol* **141**: 107113 (2021)

[23] Dai H F, Hu Y, Wu W L, Yue H X, Meng X S, Li P, Duan H G. Molecular dynamics simulation of ultra-precision machining 3C–SiC assisted by ion implantation. *J Manuf Process* **69**: 398–411 (2021)

[24] Zheng L, Chen W Q, Huo D H. Review of vibration devices for vibration-assisted machining. *Int J Adv Manuf Tech* **108**(5–6): 1631–1651 (2020)

[25] Huang W H, Yan J W. Towards understanding the mechanism of vibration-assisted cutting of monocrystalline silicon by cyclic nanoindentation. *J Mater Process Tech* **311**: 117797 (2023)

[26] Zhao Q L, Sun Z Y, Guo B. Material removal mechanism in ultrasonic vibration assisted polishing of micro cylindrical surface on SiC. *Int J Mach Tool Manu* **103**: 28–39 (2016)

[27] Chen Y, Hu Z W, Yu Y Q, Lai Z Y, Zhu J G, Xu X P, Peng Q. Processing and machining mechanism of ultrasonic vibration-assisted grinding on sapphire. *Mat Sci Semicon Proc* **142**: 106470 (2022)

[28] Huang Y H, Wang M C, Xu Y X, Zhu F L. Investigation of vibration-assisted nano-grinding of gallium nitride via molecular dynamics. *Mat Sci Semicon Proc* **121**: 105372 (2021)

[29] He Y, Sun J T, Gao P, Song S Y, Wang K Y, Tang M L. Atomic removal mechanism of nano polishing for single-crystal AlN substrate via molecular dynamics. *Mat Sci Semicon Proc* **156**: 107294 (2023)

[30] Qiao G C, Yi S C, Zheng W, Zhou M. Material removal behavior and crack-inhibiting effect in ultrasonic vibration-assisted scratching of silicon nitride ceramics. *Ceram Int* **48**(3): 4341–4351 (2022)

[31] Wang Y H, Liang Z Q, Zhao W X, Wang X B, Wang H. Effect of ultrasonic elliptical vibration assistance on the surface layer defect of M-plane sapphire in microcutting. *Mater Design* **192**: 108755 (2020)

[32] Guo J, Tan S L, Xiao C. Atomistic understanding of scratching-induced material attrition of wurtzite single-crystal AlN using nanoscale diamond abrasive. *Tribol Int* **169**: 107483 (2022)

[33] Huang W W, Tang J Y, Zhou W H, Shao W, Yi M H, Zhao X, Wen J. Revealing nanoscale material deformation mechanism and surface/subsurface characteristics in vibration-assisted nano-grinding of single-crystal iron. *Appl Surf Sci* **597**: 153692 (2022)

[34] Liu C L, He W B, Chu J N, Zhang J G, Chen X, Xiao J F, Xu J F. Molecular dynamics simulation on cutting mechanism in the hybrid machining process of single-crystal silicon. *Nanoscale Res Lett* **16**: 66 (2021)

[35] Wang H, Yang G L, Su H, Dong Z G, Guo X G, Bao Y, Zhang P F. Insight into surface formation mechanism during ultrasonic elliptical vibration cutting of tungsten alloy by scratching experiment and molecular dynamics. *Tribol Int* **191**: 109088 (2024)

[36] Wang H, Dong Z G, Wang C K, Kang R K, Guo X G, Bao Y. Surface/subsurface formation mechanism of tungsten during ultrasonic elliptical vibration cutting. *Int J Mech Sci* **262**: 108725 (2024)

[37] Zhang H, Sun C, Hong Y, Deng Y S, Ma L. Aluminium nitride surface characterization by grinding with laser-ultrasonic coupling. *Materials* **17**(15): 3772 (2024)

[38] Zhang H, Sun C, Hong Y, Deng Y S, Ma L. Aluminum nitride surface modification mechanism by laser ultrasonic-assisted grinding. *Tribol Int* **196**: 109718 (2024)

[39] Wang J Q, Yan Y D, Li C, Geng Y Q. Material removal mechanism and subsurface characteristics of silicon 3D nanomilling. *Int J Mech Sci* **242**: 108020 (2023)

[40] Wang J Q, Yan Y D, Li Z H, Geng Y Q, Luo X C, Fan P F. Processing outcomes of atomic force microscope tip-based nanomilling with different trajectories on single-crystal silicon. *Precis Eng* **72**: 480–490 (2021)

[41] Wang J Q, Yan Y D, Li Z H, Geng Y Q. Towards understanding the machining mechanism of the atomic force microscopy tip-based nanomilling process. *Int J Mach Tool Manu* **162**: 103701 (2021)

[42] Chen J Y, Zhang W X, Tong K. Effect of twins on scratching behavior of nanotwinned diamond: A molecular dynamics simulation. *Appl Surf Sci* **616**: 156545 (2023)

[43] Wang Y H, Liang Z Q, Zhao W X, Wang X B, Wang H. Anisotropic cutting mechanisms on the surface quality in ultra-precision machining of R-plane sapphire. *Appl Surf Sci* **622**: 156868 (2023)

[44] Vashishta P, Kalia R K, Nakano A, Rino J P. Interaction potential for silicon carbide: A molecular dynamics study of elastic constants and vibrational density of states for crystalline and amorphous silicon carbide. *J Appl Phys* **101**(10): 103515 (2007)

[45] Mayo S L, Olafson B D, Goddard W A. DREIDING: A generic force field for molecular simulations. *J Phys Chem* **94**(26): 8897–8909 (1990)

[46] Plimpton S. Fast parallel algorithms for short-range molecular dynamics. *J Comput Phys* **117**(1): 1–19 (1995)

[47] Stukowski A. Visualization and analysis of atomistic simulation data with OVITO—the Open Visualization Tool. *Model Simul Mater Sc* **18**(1): 015012 (2010)

[48] Stukowski A, Albe K. Extracting dislocations and non-dislocation crystal defects from atomistic simulation data. *Model Simul Mater Sc* **18**(8): 085001 (2010)

[49] Williams B E, Glass J T. Characterization of diamond thin films: Diamond phase identification, surface morphology, and defect structures. *J Mater Res* **4**(2): 373–384 (1989)

[50] Dai H F, Chen G Y, Zhou C, Fang Q H, Fei X J. A numerical study of ultraprecision machining of monocrystalline silicon with laser nano-structured diamond tools by atomistic simulation. *Appl Surf Sci* **393**: 405–416 (2017)

[51] Doan D Q, Fang T H, Tran A S, Chen T H. High deformation capacity and dynamic shear band propagation of imprinted amorphous $Cu_{50}Zr_{50}$/crystalline Cu multilayered nanofilms. *J Phys Chem Solids* **138**: 109291 (2020)

[52] Chen J J, Chen K B, Su X J, Niu M T, Wang Q Q, Xu K. Dislocation slip systems in c-plane and m-plane AlN single crystals under nano-indentation. *Thin Solid Films* **791**: 140240 (2024)

[53] Do T T, Fang T H. Atomistic analysis of the phase transformation and wear regimes of textured Wurtzite–SiC hexagonality using molecular dynamics simulation. *Tribol Int* **188**: 108907 (2023)

[54] Luo X, Zhang Z B, Xiong Y N, Shu Y, He J Z, Zheng K H, Bao Y, Urbassek H M. Atomistic simulation of amorphization during AlN nanoindentation. *Ceram Int* **47**(11): 15968–15978 (2021)

[55] Xu W H, Sheng C, Zhong M. Effects of ultrasonic vibration on sapphire polishing investigated by molecular dynamics. *Tribol Int* **176**: 107911 (2022)

[56] Li C, Hu Y X, Zhang F H, Geng Y Q, Meng B B. Molecular dynamics simulation of laser assisted grinding of GaN crystals. *Int J Mech Sci* **239**: 107856 (2023)

[57] Wang J Q, Yan Y D, Wei S P, Chen G T, Cui H L, Geng Y Q, Li C. Understanding the machining mechanism in ultrasonic vibration-assisted nanogrinding of GaN. *Mat Sci Semicon Proc* **185**: 108868 (2025)

[58] Tan S L, Guo J, Ling Q Q, Yin X L, Bai X W. Atomistic understanding toward the improved scratching properties of GaAs coated with monolayer graphene. *Mater Today Commun* **33**: 104145 (2022)

[59] Zhao X H, Zhang X S, Chen R L, Lang H J, Peng Y T. Flexible tuning of friction on atomically thin graphene. *ACS Appl Mater Inter* **15**(7): 10315–10323 (2023)

[60] Sahli R, Pallares G, Ducottet C, Ben Ali I E, Al Akhrass S, Guibert M, Scheibert J. Evolution of real contact area under shear and the value of static friction of soft materials. *P Natl Acad Sci USA* **115**(3): 471–476 (2018)

[61] Weber B, Suhina T, Junge T, Pastewka L, Brouwer A M, Bonn D. Molecular probes reveal deviations from Amontons' law in multi-asperity frictional contacts. *Nat Commun* **9**: 888 (2018)

[62] Larsson P L. On representative stress correlation of global scratch quantities at scratch testing of elastoplastic materials. *Mater Design* **49**: 536–544 (2013)

[63] Dai H F, Zhang F, Chen J B. A study of ultraprecision mechanical polishing of single-crystal silicon with laser nano-structured diamond abrasive by molecular dynamics simulation. *Int J Mech Sci* **157**: 254–266 (2019)

[64] Huang K, Yang W Y. Analytical modeling of residual stress formation in workpiece material due to cutting. *Int J Mech Sci* **114**: 21–34 (2016)

[65] Niu Y H, Zhao D, Wang S B, Li S C, Wang Z X, Zhao H W. Investigations on thermal effects on scratch behavior of monocrystalline silicon via molecular dynamics simulation. *Mater Today Commun* **26**: 102042 (2021)

[66] Rao X S, Zhang F H, Luo X C, Ding F, Cai Y K, Sun J N, Liu H T. Material removal mode and friction behaviour of RB–SiC ceramics during scratching at elevated temperatures. *J Eur Ceram Soc* **39**(13): 3534–3545 (2019)

[67] Hu Y Z, Ma T B, Wang H. Energy dissipation in atomic-scale friction. *Friction* **1**(1): 24–40 (2013)

[68] Doan D Q, Fang T H, Chen T H. Machining mechanism and deformation behavior of high-entropy alloy under elliptical vibration cutting. *Intermetallics* **131**: 107079 (2021)

[69] Wu Y Q, Mu D K, Huang H. Deformation and removal of

semiconductor and laser single crystals at extremely small scales. *Int J Extreme Manuf* **2**(1): 012006 (2020)

[70] Xie W K, Fang F Z. Effect of tool edge radius on material removal mechanism in atomic and close-to-atomic scale cutting. *Appl Surf Sci* **504**: 144451 (2020)

[71] Zhao Y T, Wang Q K, Li Z, Fu D Y, Zhang G, Wu J, Ren Z M. Molecular dynamics simulations of the thermally and stress-activated glide of a $\langle 0001\rangle\{1\bar{1}00\}$ screw dislocation in AlN. *Cryst Growth Des* **21**(10): 5614–5620 (2021)

Shuaicheng Feng is a graduate student at the University of South China, China, majoring in mechanical engineering. His research areas are nanotribology and ultraprecision surface machining.

Jian Guo received his Ph.D. degree in mechanical design and theory from Southwest Jiaotong University, China, in 2014. He joined the University of South China, China, in 2017. His current position is as a professor. His research areas cover tribology/nanotribology and ultraprecision surface machining.

Chen Xiao earned his Ph.D. degree in mechanical design and theory from Southwest Jiaotong University, China, in 2019. After four years at the Advanced Research Center for Nanolithography (ARCNL), the Netherlands, as a postdoctoral researcher, he joined Southwest Jiaotong University, China, in 2024 as a professor. His research is focused on micro/nanotribology.